RSC Advances

PAPER

View Article Online
View Journal | View Issue

Cite this: *RSC Adv.*, 2017, **7**, 17279

A reusable surface-quaternized nanocellulose-based hybrid cryogel loaded with N-doped TiO_2 for self-integrated adsorption/photo-degradation of methyl orange dye†

Yufei Chen,[a] Hongzhi Liu,*[ab] Biyao Geng,[a] Jing Ru,[a] Chen Cheng,[a] Ying Zhao*[a] and Likui Wang*[c]

In this work, an easily recyclable surface-quaternized nanofibrillated cellulose (Q-NFC)-based hybrid cryogel loaded with N-doped TiO_2, was fabricated through a facile one-pot hydrothermal treatment followed by freeze-drying. Due to the web-like network structure consisting of many densely entangled nanofibrils, the Q-NFC was able to act as a "green" template for supporting N-doped TiO_2. The physicochemical characteristics and micro-structure as well as the MO adsorption/photo-degradation properties of the resultant hybrid cryogels were characterized. It was demonstrated that quaternary ammonium groups anchored onto the surfaces of a Q-NFC backbone were responsible for the modest adsorption of the N-doped hybrid cryogel toward the anionic dye, whereas doping with N species enhanced the photo-catalytic activities of loaded anatase TiO_2 on MO under the irradiation of simulated solar light. Furthermore, the N-doped hybrid cryogel with mechanical durability demonstrated an excellent self-integrated removal percentage of MO (more than 99%) as well as reusability during multiple adsorption/photo-degradation cycles. Its advantages would make the cryogel an eco-friendly alternative for the harmless treatment of dye pollutants without causing a second pollution. Finally, the possible photo-degradation mechanism of MO was presented on the basis of the optical and electrochemical properties.

Received 11th January 2017
Accepted 14th February 2017

DOI: 10.1039/c7ra00450h

rsc.li/rsc-advances

1. Introduction

Dyeing effluents discharged from various industries such as textile, paper, tanneries, *etc.*, are becoming one of the major sources of water pollution and have serious impacts on ecological systems, even endangering human health.[1] Therefore, there is significant interest in the development of efficient techniques for the treatment of dye pollutants.[2]

Among a variety of established treatment strategies,[3–5] adsorption is generally recognized to be one of the most cost-effective methods for the removal of dye pollutants from aqueous wastewater (especially at low concentrations of dye molecules).[6] To date, various types of adsorbents such as activated carbon,[7] inorganic minerals,[8] and chitosan,[9] have emerged and their removal abilities for dyes have been extensively studied. However, these conventional adsorbents tend to suffer from some drawbacks, such as high cost, inferior adsorption capacity, poor recyclability for reuse, and undesired biodegradability.[10–12] Therefore, considerable attention has been recently devoted to the development of easily recyclable bio-sorbents with excellent adsorption performance.[13]

As a 'young' third generation of cryogel-type materials succeeding silica and synthetic polymer-based ones, cellulose cryogels combine the intriguing features of highly interconnected porous cryogel-type materials with the additional advantages of 'green' cellulose, such as abundant sources, natural renewability, biodegradability, and ease of surface modification due to the presence of abundant hydroxyls.[14] Moreover, as compared to conventional particulate or powdered bio-sorbents for the removal of dyes, cellulose cryogels are more easily recycled for reuse, which is more favorable in practical applications. Therefore, the latter would be able to act as promising bio-sorbents[15] as well as template materials, to immobilize photo-catalysts for the application of organic pollutant degradation.[16] The pioneering cellulose cryogels are predominantly based on regenerated cellulose (RC), and so are RC cryogels.[17,18] However, the dissolution, gelation, and solvent-exchange steps required for the preparation of RC cryogels are very cumbersome, and

[a]*School of Engineering, Zhejiang Agriculture and Forestry University, Lin'an, Hangzhou, Zhejiang Province, 311300, China. E-mail: hzliu@iccas.ac.cn*
[b]*National Engineering and Technology Research Center of Wood-based Resources Comprehensive Utilization, Lin'an, Hangzhou, Zhejiang Province, 311300, China*
[c]*School of Chemical and Materials Engineering, Jiangnan University, Wuxi, Jiangsu Province, 214122, China. E-mail: lkwang@jiangnan.edu.cn*

† Electronic supplementary information (ESI) available. See DOI: 10.1039/c7ra00450h

harmful or toxic solvents are required.[19] Moreover, the native cellulose-I crystalline structure is converted to the less strong cellulose-II one after the dissolution and regeneration,[20] thereby yielding fragile cryogels with lower aspect ratios and rod-like structures of the fibrils and fibril networks upon drying.[17,21]

Compared to RC cryogels, the cryogels based on nanofibrillated cellulose (NFC) are prepared from the direct drying of NFC suspensions, and no complicated regeneration steps and harmful solvents are involved. Thus, the latter cellulose cryogels appear more environmentally friendly. Besides, as one sub-class of nanocellulose materials, NFC is extracted from native cellulose fibers through mechanical disintegration.[22] In order to reduce the energy required for mechanical disintegration, cellulose pulps have been subjected to enzymatic pretreatment[23] or chemical pretreatment to introduce surface charge moieties.[24,25] NFC is characterized by an entangled network structure consisting of many long and flexible native cellulose nanofibers (3–60 nm in diameter).[26,27] Such unique structure also renders NFC-based cryogels with improved mechanical integrity and flexibility;[19,28] advantages which would be desirable for reusability. Thus, NFC-based cryogels would be promising dye-adsorbent materials from the viewpoint of environmental friendliness.[10,29]

Chen *et al.*[30] prepared NFC cryogels from different types of aqueous NFC suspensions with different morphologies and surface properties through freeze-drying, and compared their adsorption capacity for methylene blue (MB). After the introduction of carboxylate groups on the surface of NFC through TEMPO-oxidation pre-treatment, the amount of adsorbed dye was increased from 2.9 to 3.7 mg g^{-1} for MB. But its overall adsorption capacity was relatively low. To enhance adsorption capacities for anionic dyes, Pei *et al.*[24] prepared cellulose nanopapers based on quaternized NFCs containing trimethylammonium groups on the surfaces of the cellulose nanofibrils. It was found that its adsorption capacity for anionic dyes was directly proportional to the content of positive charges anchored onto the surface of the NFC. However, the studies above have never dealt with the post-treatment of the adsorbed dye, considering that a second pollution could occur during the subsequent disposal of dye-saturated adsorbents.

The development of reusable NFC-based cryogel materials that are able to achieve self-integrated adsorption/photo-degradation elimination of adsorbed dyes in an efficient and clean manner, would be of great interest in the treatment of dyes in wastewater. Among many photocatalysts, TiO_2 is one of the most widely used because of its low cost, non-toxicity, high chemical inertness, and strong oxidizing power.[31,32] To overcome the difficulty in recollecting and removing TiO_2 in dye-containing wastewater after photocatalytical treatment, Kettunen *et al.*[33] coated a thin TiO_2 film on an NFC cryogel *via* chemical vapor deposition (CVD). It was found that the photocatalytic degradation activity of the resultant hybrid cryogel for MB reached 70% after 24 h of UV illumination. However, pure TiO_2 photo-catalysts only absorbed the UV light that accounted for only 4% of the total solar radiation,[34] which thus largely limited the photo-degradation applications under sunlight irradiation. Furthermore, the absence of active adsorbed groups on the surfaces of the NFC cryogel limited the adsorption properties for dyes.

Within this context, the objective of this work is to utilize "green" and positively charged Q-NFC as a favorable supporting backbone for N-doped TiO_2 photocatalyst, to construct a reusable cryogel-type material with enhanced visible-light response for self-integrated adsorption/photo-degradation treatment of methyl orange (MO) which was chosen as a model anionic dye. For this purpose, surface-quaternized NFC (Q-NFC) with a densely entangled nanofibril network was first isolated from inexpensive and sustainable bamboo pulp. The surface characteristics and morphologies of the bamboo-derived Q-NFC suspension were investigated in terms of conductometric titration, zeta potential measurement, and transmission electron microscopy (TEM). Then, both TiO_2 and N species were co-incorporated into the nanofibrillar backbone of the as-prepared Q-NFC through a facile one-pot hydrothermal treatment, and then after freeze-drying the reaction mixture, the Q-NFC hybrid cryogel loaded with N-doped TiO_2 was obtained. The micro-structure as well as the adsorption and photo-degradation properties of the resultant N-doped hybrid cryogel on MO, were well characterized. Furthermore, its cyclic adsorption/photo-degradation effects on MO as well as the possible photo-degradation mechanism were studied. To our knowledge, there have never been any similar reports regarding the use of surface-charge functionalized NFC-based hybrid cryogels loaded with N-doped TiO_2 toward an efficient self-integrated adsorption/photo-degradation treatment of dye pollutants.

2. Experimental

2.1 Materials

Dried bamboo kraft pulp was commercially supplied by Sichuan Yongfeng paper Co., Ltd (China). 2,3-Epoxypropyltrimethylammonium chloride (EPTAC, technical grade) was purchased from Ji'nan Europe Trade Co., Ltd. Sodium hydroxide, titanium sulfate ($Ti(SO_4)_2$), urea, and methyl orange were of chemical grade and supplied by Sinopharm Chemical Reagent Co., Ltd (China).

2.2 Preparation of Q-NFC from bamboo pulp

The bamboo pulp was first subjected to the pre-treatment of mechanical beating in a laboratory PFI-mill. The pre-treated pulp was mixed with a sodium hydroxide solution to obtain a suspension with the concentrations of both pulp and NaOH equal to 5 wt%. Subsequently, the desired amount of EPTAC (2.9 g per gram of the pulp) was added to the suspension under magnetic stirring and the reaction was carried out at 65 °C for 8 hours. After the completion of the reaction, the mixture was neutralized with diluted hydrochloric acid, filtered, and then thoroughly washed with deionized water. The resultant fiber pulp was passed through a high-pressure homogenizer for three cycles at a pressure of 500 bar at ambient temperature. A transparent dispersion of Q-NFC was ultimately obtained.

2.3 Preparation of hybrid cryogels

Nitrogen-doped TiO_2/Q-NFC hybrid cryogels (designated as '*x*NyTi–NFC', where *x* and *y* represent the weight ratios of N and Ti, respectively, with respect to the amount of solid Q-NFC) were prepared through a facile one-pot hydrothermal strategy. First, a diluted Q-NFC suspension was condensed to a solid content of 0.45 wt% using a rotary evaporator. Then, 55 g ethanol was added into 30 g condensed Q-NFC suspension that was subsequently subject to sonication until a homogenous mixture was achieved. The $Ti(SO_4)_2$ and urea as TiO_2 and N precursors were dissolved into 5 g ethanol and 1 mL deionized water, respectively, and added to the above Q-NFC suspension. After being stirring vigorously for 2 hours, the aqueous mixture was immediately transferred into an autoclave for hydrothermal treatment at 120 °C for 4 h. The reaction mixture was filtered and then thoroughly washed with deionized water five times. After 10 mL deionized water was added, the mixture was sonicated for 30 min until a homogenous state was achieved. The as-obtained gel was then freeze-dried at −60 °C into the cryogel. For comparison, Q-NFC cryogels doped with urea or TiO_2 (labeled as '*x*N-NFC' and '*y*Ti-NFC', respectively), N-TiO_2, and an unmodified Q-NFC one, were also prepared under the same conditions. Furthermore, 10N10Ti–NFC with oven drying was also prepared.

2.4 Characterization

2.4.1 Characterization of Q-NFC. The quaternary ammonium group content of Q-NFC was estimated through conductometric titration of chloride ions with $AgNO_3$ standard solution.[24] Typically, the dried Q-NFC sample (100 mg) was dispersed in 100 mL Milli-Q water, and titrated with 8 mM aqueous $AgNO_3$ solution by adding 0.2 mL in 60 second intervals. Assuming the presence of one chloride counter-ion per trimethylammonium group, the amount of trimethylammonium groups, C (mmol g^{-1}), was calculated according to the equation below:

$$C = \frac{(V_1 - V_0) \times C_{AgNO_3}}{m} \quad (1)$$

where $(V_1 - V_0)$ is the consumed volume of $AgNO_3$ solution; C_{AgNO_3} is the exact concentration of $AgNO_3$ solution; and m is the weight of the dried NFC sample.

The zeta potential of a 0.1 wt% suspension of Q-NFC (pH = 7) was measured using a ZetaPALS (Brookhaven, USA) at 25 °C. The measurements were performed for five repeats for each sample, and the corresponding average values were reported together with the standard deviation. A droplet of very diluted Q-NFC dispersion (*ca.* 0.01 wt%) was deposited onto a carbon-coated copper grid. The excess liquid was blotted with a piece of filter paper, and a droplet of 1% uranyl acetate solution was added prior to drying. The negatively stained specimens obtained were observed using TEM (JEM-1200EX, JEOL, Japan) at an accelerating voltage of 80 kV.

2.4.2 Characterization of the cryogels. The morphologies of the cryogel samples were observed using a JEM-1200EX transmission electron microscope (JEOL, Japan) at an accelerating voltage of 80 kV and a Nova NanoSEM 450 SEM apparatus (FEI, Japan) at an accelerating voltage of 15 kV, respectively. Prior to SEM observation, the surface of the samples were sputter-coated with a thin layer of platinum to avoid charging. The energy-dispersive X-ray microanalysis (EDX) was measured using a Nova NanoSEM 450 scanning electron microscopy apparatus (FEI, Japan) at an accelerating voltage of 30 kV.

Wide-angle X-ray diffraction (WAXD) patterns were collected at a diffraction angle of 2θ = 10–60° on an XRD 6000 diffractometer (Shimadzu, Japan) with Cu Kα radiation (λ = 1.5406 Å) operated at 40 kV and 30 mA. Fourier transform infrared (FT-IR) spectra were recorded on an IR Prestige-21 infrared spectrometer (Shimadzu, Japan) in the wavenumber range of 4000–400 cm^{-1} at a resolution of 4 cm^{-1} and 32 scans. The samples were ground with pre-dried KBr powder and then compressed into disks for FT-IR tests. UV-visible absorbance spectra were collected using a UV-1800 model UV/Vis spectrophotometer (Shimadzu, Japan). X-ray photoelectron spectroscopy (XPS) signals were collected on an AXIS-ULTRA DLDVG-type instrument (Shimadzu/Kratos, Japan).

N_2 adsorption–desorption experiments were performed on an Autosorb-IQ2-MP-XR-VP porosity and specific surface area analyzer (Quantachrome, America) with the sample degassed at 150 °C for 3 h before the test. The specific surface area was calculated using the Brunauer–Emmett–Teller (BET) method.

The calibration curve for MO concentrations was pre-established by drawing a straight line for the absorbance at λ_{max} = 464 nm against a series of known MO concentrations. All of the adsorption tests of MO were performed at 20 °C. Typically, about 50 mg cryogel sample was added into 50 mL aqueous MO (10 mg L^{-1}) solution under magnetic stirring. At the predetermined time interval, 1 mL of the aliquot solution was sampled and immediately analyzed using the established calibration curve on a Shimadzu UV-1800 UV/Vis spectrophotometer to determine the variation of MO concentration as a function of adsorption time. The adsorption kinetics of MO by 10N10Ti–NFC were studied by fitting the curves with both kinetic models, respectively, *i.e.* the pseudo-first-order model and pseudo-second-order one as expressed by eqn (2) and (3):

Pseudo-first-order:

$$\ln(q_e - q_t) = \ln q_e - k_1 t \quad (2)$$

Pseudo-second-order:

$$\frac{t}{q_t} = \frac{1}{k_2 q_e^2} + \frac{t}{q_e} \quad (3)$$

where q_t represents the adsorption at t time (min), and q_e represents the adsorption capacity at the equilibrium; k_1 and k_2 are the kinetic rate constants for the pseudo-first and second order models, respectively.

Furthermore, Langmuir and Freundlich were used to obtain the isotherm parameters (including the maximum adsorption capacity) for adsorption of MO onto 10N10Ti–NFC. This can be expressed as the following equations:

Langmuir equation:

$$\frac{c_e}{q_e} = \frac{1}{K_L q_{max}} + \frac{c_e}{q_{max}} \quad (4)$$

Freundlich equation:

$$\log q_e = \log K_F + \frac{\log c_e}{n} \quad (5)$$

where q_e is the amount of solute adsorbed at equilibrium per unit weight of adsorbent (mg g^{-1}), c_e is the equilibrium concentration of solute in the bulk solution (mg L^{-1}), q_{max} is the maximum adsorption capacity (mg g^{-1}), K_L is the constant related to the free energy of adsorption, K_F is the constant indicative of the relative adsorption capacity of the adsorbent and $1/n$ is the constant indicative of the intensity of the adsorption.

The photo-catalytic activity of the samples was evaluated through the photo-degradation of MO under the simulated solar light. For a typical process, approximately 50 mg cryogel sample was added to the cylindrical quartz tube containing 50 mL MO solution (10 mg L^{-1}). Prior to the irradiation, the solution was magnetically stirred in the dark for 30 min to reach the adsorption/desorption equilibrium of MO between the cryogels and MO dye. The stirred suspension was irradiated with a 300 W high-pressure Xe lamp equipped with an optical filter (AM 1.5) and an emission wavelength range of 200–800 nm. Under the irradiation, about 4 mL of aliquot solution were taken out at each pre-determined time interval and the change of MO concentration with time was determined using a Shimadzu UV-1800 UV/Vis spectrophotometer at λ_{max} = 464 nm. After the irradiation, the samples were transferred into 50 mL deionized water and then irradiated under the same light source for 30 min to regenerate the cryogel. Its cyclic adsorption/photo-degradation properties were measured using the same method as described above.

To account for the photocatalytic mechanism, cyclic voltammetry (CV) and electrochemical impedance spectroscopy (EIS) of the doped cryogel samples were carried out on a classical three-electrode system using a Zahner electrochemical station. The supporting electrolyte was the mixed solution of 2.5 mmol L^{-1} $K_3Fe(CN)_6$, $K_4Fe(CN)_6$, and 0.1 mol L^{-1} KCl. A platinum electrode, saturated calomel electrode (SCE), and FTO glasses coated with thin sample films, were used as the counter, reference, and working electrodes, respectively. The electrode potential was 0.2 V *versus* SCE. The scan rate of CV was set at 100 mV s^{-1} and the frequency ranged from 0.1 to 106 Hz for EIS.

3. Results and discussion

3.1 Morphologies of Q-NFC

Q-NFC suspension was prepared *via* mechanical disintegration of kraft bamboo pulp, which was pre-treated through the reaction with EPTAC in the presence of sodium hydroxide. The zeta-potential value of the NFC suspension was determined to be 40.33 ± 0.94 mV, suggesting excellent dispersion stability of cellulose nanofibers in water. The content of trimethylammonium chloride group was determined to be 0.50 ± 0.02 mmol g^{-1} using a conductometric titration method.

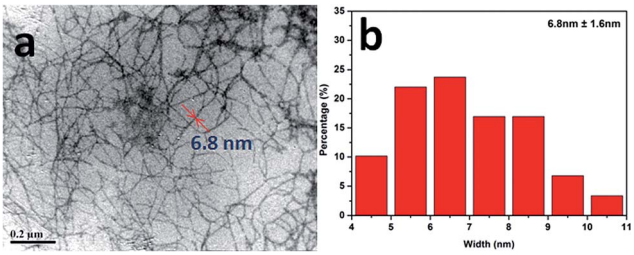

Fig. 1 (a) Stained TEM micrograph of the quaternized NFC dispersion isolated from bleached bamboo pulp; (b) the width distribution histogram of its nanofibrils.

Fig. 1a shows the negatively stained TEM micrograph of the Q-NFC dispersion isolated from bamboo pulp. The flexible and entangled network structure comprising many long and randomly distributed sub-micron fibrils is clearly shown. Based on the estimated width distribution histogram of the nanofibrils (Fig. 1b), the average width was calculated to be 6.8 ± 1.6 nm for Q-NFC. This result clearly indicated that the bamboo pulp fibers were successfully nanofibrillated due to the presence of surface positively-charge moieties. However the Q-NFC derived from bamboo pulp exhibited more densely entangled and crimpy nanofibrils with quite non-uniform width, which was somewhat different from the ones from softwood pulp in the previous report.[24] Such an entangled network would act as a good template to load nano-sized TiO_2 photocatalysts or other species.

3.2 Structure analysis of Q-NFC based cryogels

Since the photocatalytic activity of TiO_2 depends largely on its state of dispersion, the micro-structure of the cryogel samples

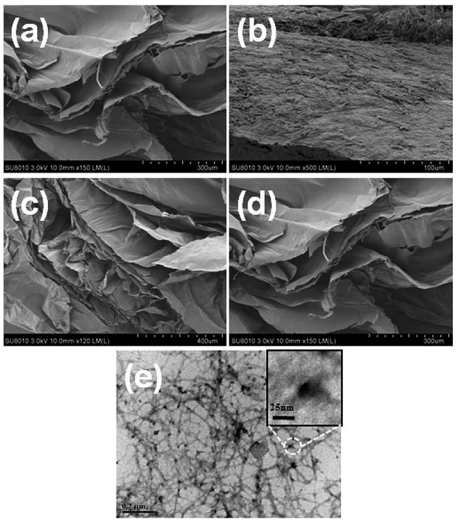

Fig. 2 SEM images of Q-NFC (a), 10N–NFC (b), 10Ti–NFC (c), and 10N10Ti–NFC (d) cryogels together with a TEM image of 10N10Ti–NFC (e).

were examined using SEM. As shown in Fig. 2a–d, all of the samples displayed an interconnected porous structure composed of many thin sheets. These thin sheets were considered to result from the self-assembly aggregation of cellulose nanofibrils during the freezing step, when the ice crystals formed.[35,36] Compared to the other cryogel samples, the sheet surfaces of the 10N–NFC appeared less smooth (as shown in Fig. 2b). This may be due to a relatively higher content of N species covering the surfaces of cellulose nanofibrils in this case. From the TEM image of the 10N10Ti–NFC cryogel (Fig. 2e), one can clearly note that there were many dark dots of 20–40 nm in size, which were uniformly decorated on the surfaces of nanofibrils. These dots should be attributed to the *in situ* formed TiO_2 nanoparticles during the hydrothermal treatment.

Fig. 3 shows the energy-dissipative X-ray (EDX) spectra of these Q-NFC based cryogels, and their weight percentages of four elements are summarised in Table 1. As one expected, the un-modified Q-NFC cryogel displayed both C and O peaks, while the additional Ti peak was noted for 10Ti–NFC. But there was no N detected in both of the samples despite the presence of quaternary trimethylammonium groups on their surfaces. This might be attributed to the very low amount of N in the Q-NFC itself ($\leq$0.7 wt%), which might be below the lower limit of EDX detection. Compared to the Q-NFC aerogel, however, the 10N–NFC one had an N content of *ca.* 3.39 wt%, suggesting the incorporation of N species into the Q-NFC backbone. For the 10N10Ti–NFC sample, remarkably lower content of Ti and N elements with respect to 10Ti–NFC or 10N–NFC were found although equal dosages of $Ti(SO_4)_2$ and urea were added in these cases. This might suggest that the simultaneous incorporation of $Ti(SO_4)_2$ and urea would adversely affect the immobilization of either species on the Q-NFC backbone. One possibility may be that some portions of Ti^{4+} combined with urea to form the complex compound rather than covalently bonding with Q-NFC during the hydrothermal treatment, resulting in some loss of both Ti and N during the subsequent filtration step.

Fig. 4a presents the wide-angle X-ray diffraction (WAXD) patterns of bamboo pulp and the cryogel samples. All five samples exhibited the main diffraction signals at 2θ = 16.5°, 22.5°, and 34.5° (indicated with the symbol "Δ"), which are characteristic of typical cellulose-I crystals.[37] When Ti species were incorporated into the Q-NFC cryogel, the diffraction peaks at 2θ = 25.3°(101), 48.1°(200), and 53.9°(105) indicated by the symbol "O", appeared for both 10Ti–NFC and 10N10Ti–NFC samples. This confirmed the formation of anatase TiO_2 phase during the hydrothermal treatment. However, the intensities of the anatase phase were not very prominent because the content of incorporated Ti species was still relatively low for these samples.

Table 1 Element compositions of four Q-NFC-based cryogels determined using EDX

Samples	C (wt%)	O (wt%)	N (wt%)	Ti (wt%)
Q-NFC	49.54	50.46	0	0
10N–NFC	48.50	48.11	3.39	0
10Ti–NFC	44.1	49.65	0	6.25
10N10Ti–NFC	60.56	36.57	1.85	1.02

UV-Vis absorption spectra of the Q-NFC and Q-NFC based samples are illustrated in Fig. S1.† A similar spectra pattern was found for both Q-NFC and 10N–NFC cryogel samples, both of which did not show perceptible absorption peaks in the wavelength range of 400–800 nm. However, both 10Ti–NFC and 10N10Ti–NFC cryogels exhibited a pronounced absorption in the UV region. This was mainly attributed to the presence of TiO_2 nanoparticles in these samples. Therefore, this result suggested that Ti species has been incorporated into the framework of the Q-NFC cryogels.[38] And as compared to 10Ti–NFC, the 10N10Ti–NFC cryogel shows a red shift in its UV absorption spectra, which may arise from the doping of nitrogen in the TiO_2 lattice.[39]

To further gain an insight into the molecular interactions between the constituents, FT-IR spectra of the cryogel samples are shown in Fig. 4b. Both Q-NFC and 10Ti–NFC cryogels showed a moderate peak at 1640 cm^{-1} that was associated with the O–H bending vibration of the absorbed moisture. But a sharper peak at 1643 cm^{-1} was visible for 10N–NFC and 10N10Ti–NFC and likely stemmed from the characteristic absorption of an amide-I (–C(=O)–NH–) band[40] that overlapped with the O–H bending vibration of the absorbed moisture. And another less intense band at 1554 cm^{-1} was attributed to the amide-II vibration. These results evidenced the incorporation of N species (*i.e.* urea) into the Q-NFC cryogel backbone. The peaks

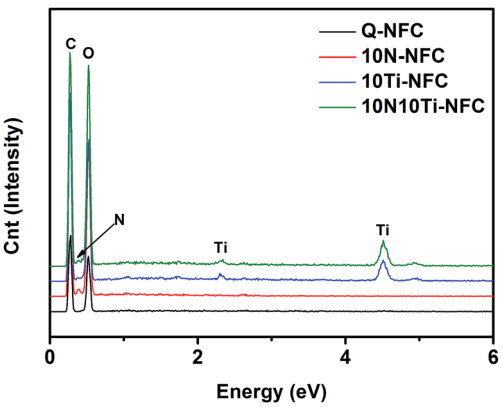

Fig. 3 EDX element spectra of the Q-NFC cryogel and the hybrid cryogels.

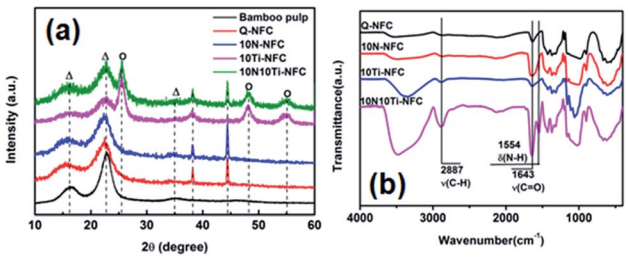

Fig. 4 Wide-angle XRD patterns (a) and FT-IR spectra (b) of various Q-NFC-based cryogel samples.

at 3358 cm^{-1} and 2887 cm^{-1} were evident for both 10Ti–NFC and 10N10Ti–NFC cryogels, and were attributed to the stretching vibration of O–H[41] and C–H,[42] respectively. The increased intensity of –OH stretching vibration might arise from the additional contribution from hydroxyl groups on the surfaces of TiO_2.

Fig. S2† presents the high-resolution C1s, O1s and N1s XPS spectra of 10N10Ti–NFC cryogel. As shown in Fig. S2a,† the C1s peak can be resolved into four peaks (*i.e.* 284.6, 285.8, 287.1, and 289.8 eV) which were assigned to C–C–OH bonding, O–C–O or C═O bonding, C–O–C bonding, and O–C–O or C═O bonding, respectively. This indicated that the carbon atoms derived from the NFC backbone.[43–45] For the O1s XPS spectrum (Fig. S2b†), the peaks of binding energy at 529.3 and 532.3 eV, were assigned to the bonds of Ti–O and O–H associated with the oxygen and/or water absorbed on the sample surface, respectively. A bimodal peak located at about 399.7 and 402.8 eV appeared in the N1s spectrum (Fig. S2c†) of the 10N10Ti–NFC sample. It has been reported that the peak at *ca.* 399.6 eV is a sign of N doping inside the lattice of titanium, which can be attributed to Ti–O–N or Ti–N–O.[46] This bonding structure could form a narrow band gap that induced visible-light catalytic activity.[47–49] The peak at 402.8 eV resulted from the adsorbed N_2.[50]

3.3 Adsorption and photo-catalytic activities for MO dye

The dependence of MO removal percentage as a function of contact time is shown in Fig. 5. It was revealed that adsorption equilibrium for Q-NFC and Q-NFC-based cryogels in 10 mg L^{-1} of MO was almost attained within 20 minutes. Among them, the virgin Q-NFC cryogel exhibited the optimum adsorption capacity for MO in the dark with a removal percentage of MO equal to 84.8%. And upon the addition of either Ti or N species, the adsorption capacity of Q-NFC cryogel was deteriorated to some extent and the removal percentage of MO was equal to 45.0% for 10Ti–NFC and 61.0% for 10N–NFC. This may be attributed to the shielding of surface cationic groups in the Q-NFC cryogels by the introduced TiO_2 or N species. When both TiO_2 and N species were simultaneously incorporated into Q-NFC template, however, the adsorption capacity of the resultant 10N10Ti–NFC cryogel became slightly higher than the 10Ti–NFC one but lower than 10N–NFC. This may be attributed to the occurrence of a combination of N species with TiO_2, which partially weakened the masking effect of either species on positively charged groups on the surfaces of the Q-NFC cryogel. But a further increase in the amounts of N or Ti species resulted in a pronounced decline in the adsorption capacity of MO.

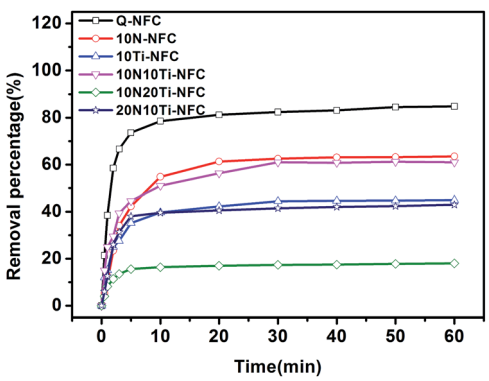

Fig. 5 Removal percentages of Q-NFC and Q-NFC based cryogels toward MO as a function of time at 20 °C in the dark (note: the initial concentration of MO was 10 mg L^{-1} and the adsorbent dosage was 1 g L^{-1}).

Since the adsorption capacity of the adsorbents toward dyes was largely dependent of their specific surface area,[51] the BET specific surface areas of the Q-NFC based cryogels were measured and the results are outlined in Table S1.† It can be seen that the BET specific surface area of all of the cryogels ranged from 16–25 $m^2 g^{-1}$. A such the low specific surface area has been attributed to the aggregation of nanofibrils into thin sheets during the freeze-drying step.[36,52] Similar specific surface area values were also observed for other NFC cryogels prepared *via* freeze-drying of aqueous NFC suspensions.[53,54] Upon the incorporation of N or Ti species into the Q-NFC cryogel, the specific surface area was slightly decreased, indicating a reduced void volume fraction within the cryogels. It can conclude that the positively-charged groups on the surfaces of the Q-NFC based cryogels rather than specific surface area could play a predominant role in determining their adsorption capacity for MO. Based on the consideration of the balance between adsorption and photo-degradation properties, the 10N10Ti–NFC cryogel was utilized to subsequently investigate the adsorption and photo-degradation properties of the N-doped Q-NFC/TiO_2 hybrid cryogel on MO dye.

In order to clarify the adsorption mechanism of the 10N10Ti–NFC cryogel toward MO dye, the collected data above were fitted with Lagergren pseudo-first-order and pseudo-second-order models. The fitting curves of both kinetic models are shown in Fig. S3a and b† and the calculated parameters are listed in Table 2. It was found that the correlation coefficient value (R^2) for the pseudo-second-order adsorption model was much higher than that of the pseudo-first-order adsorption one. Moreover, the adsorption equilibrium value (q_e) calculated from the former model was quite close to the measured data. The results evidenced that the adsorption process of the 10N10Ti–NFC aerogels for MO dye was dominated by chemical adsorption. In some previously reported nanocellulose-based adsorbents with negatively charged groups anchored onto their surfaces,[51,55] the adsorption process for cationic dyes predominantly driven by electrostatic interaction was also found to follow a pseudo-second-order adsorption kinetic model.

Furthermore, the Langmuir and Freundlich isotherm plots for the adsorption of MO on 10N10Ti–NFC are shown in

Table 2 Model-fitting kinetic parameters for the MO adsorption of 10N10Ti–NFC cryogel

Kinetic models	q_e (mg g^{-1})	K (g (mg min)$^{-1}$)	R^2
Pseudo-first-order	4.021	0.172	0.762
Pseudo-second-order	6.383	0.074	0.999

Fig. S4.† The high correlation coefficient (R^2 = 0.9997) demonstrated that the Langmuir model provided a good theoretical correlation to the adsorption equilibrium, indicating that the adsorption of this cryogel followed the monolayer surface coverage in the dye concentration range studied. And the theoretical maximum adsorption capacity for MO was determined to be 17.6 mg g^{-1}. The modest adsorption capacity toward anionic dyes in our hybrid NFC cryogel was likely attributed to the fact that the Q-NFC used in our work had an evidently lower quaternary group content than those in Pei's work (0.5 *vs.* 2.31 mmol g^{-1}).[24] In addition, the shielding effect of incorporated TiO_2 and N species on the Q-NFC hybrid cryogel would reduce the content of accessible positively-charged moieties to MO. It should be pointed out that this study paid attention to the self-cleaned elimination of MO dye through the integrated adsorption/photo-degradation cycles under sunlight irradiation rather than the sole adsorption of the dye.

The photo-catalytic activities of Q-NFC and Q-NFC based cryogel samples were evaluated by exposing them to the irradiation of simulated solar light, as shown in Fig. 6a. As a control test, the MO dye itself only degraded by a very small amount without the incorporation of TiO_2. And the pure Q-NFC cryogel showed the maximum adsorption efficiency, but its adsorbed MO dye could hardly be degraded under the irradiation of simulated solar light, and was still dark orange (Fig. 6b). Both 10N–NFC and 10Ti–NFC ones exhibited poor photo-degradation activity as well. The optimum degradation effect was noted for the 10N10Ti–NFC and 10N20Ti–NFC cryogels, confirming the role of N-doping in improving the photo-degradation performance of the TiO_2-supported Q-NFC cryogels. As shown in Fig. 6c, the white 10N10Ti–NFC cryogel became deep orange after the immersion into the MO solution for 30 min. More than half of the dye was adsorbed by the cryogel (Fig. 6a) and the orange color of the liquid became lighter than that of the hybrid cryogel (Fig. 6c). After the irradiation for 90 min, the solution turned into totally colorless, while the cryogel itself appeared very slightly orange (Fig. 6c). The N-doped hybrid cryogel can be recovered to be colorless after regeneration, indicative of its good self-cleaning properties. At a fixed nitrogen content, an increase in the content of titanium remarkably accelerated the photo-degradation rate, while the photo-degradation effect became worse on increasing the content of nitrogen under the same titanium content (Fig. 6a). This result indicated that the N/Ti ratio in the hybrid cryogels was crucial in determining the degradation efficiency of MO dye.

The photo-degradation performance of 10N10Ti–NFC was further compared with N-TiO_2 and oven-dried 10N10Ti–NFC as control samples (Fig. S5†). It can be noted that the final photo-degradation efficiency of 10N10Ti–NFC was close to that of N-TiO_2. But the adsorption capacity of 10N10Ti–NFC was obviously higher than that of N-TiO_2, which was evidently attributed to the presence of the Q-NFC component in the former. To reveal the role of the porous structure on the adsorption and photo-degradation performance, the 10N10Ti–NFC sample was also prepared through oven-drying and the result is presented in Fig. S5.† Compared to the freeze-dried sample with the interconnected porous structure, the oven-dried one with the compact one showed a much poorer adsorption capacity and photo-degradation performance. This was possibly because it was hard for MO molecules to penetrate inside in the latter case so that the contact of the dyes with the internal active adsorption and photo-catalytic sites was drastically reduced.

Furthermore, the adsorption-degradation process of the 10N10Ti–NFC sample was monitored at different solution pH values (Fig. S6†). Its adsorption and degradation performances under either alkaline or acidic conditions were lowered at varying levels compared to those under neutral conditions. At the low pH values, this decrease in the adsorption and degradation performances was presumably caused by the higher competition between the dye molecules and H^+ ions to form electrostatic attraction. The decrease at high pH values was attributed to the competition between dye active adsorption sites and OH^- ions to form electrostatic attraction. As a result, fewer dye molecules were able to contact TiO_2 in both cases.

Fig. 7 further shows the reusability of the 10N10Ti–NFC cryogel after multiple adsorption/photo-degradation cycles of

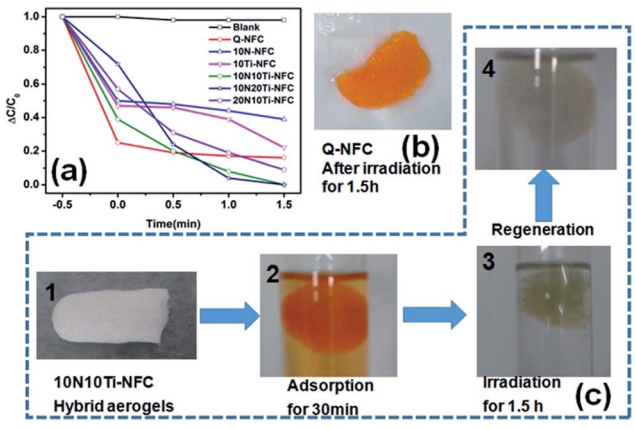

Fig. 6 (a) The photo-degradation performance of the Q-NFC based cryogel samples under the irradiation of simulated solar light; (b) the photograph of pure Q-NFC cryogel after irradiation for 1.5 h; (c) the photographs of adsorption–degradation–regeneration processes of the 10N10Ti–NFC cryogel.

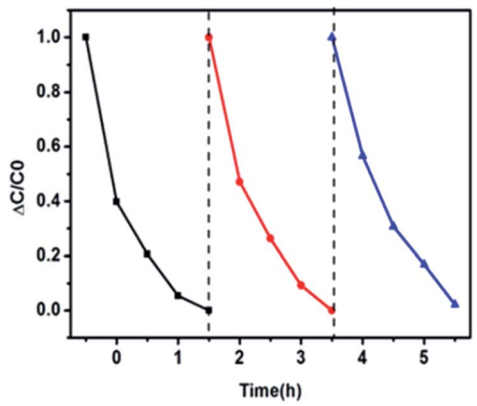

Fig. 7 The recycling adsorption/photo-degradation performance of 10N10Ti–NFC towards MO under the irradiation of simulated solar light.

MO. It can be noted that the 10N10Ti–NFC cryogel still maintained relatively preferable photo-catalytic activity after three cycles. The MO solution was able to be completely degraded within 90 min. Therefore, the N-doped TiO_2/Q-NFC hybrid cryogel exhibited good integrated adsorption/photo-degradation performance toward MO. However, the equilibrium adsorption capacity in the darkness was somewhat weakened. For example, the adsorption capacity at the 3rd cycle was somewhat decreased by about 25% relative to the 1st cycle. This was presumably attributed to the possibility that it was hard for the simulated solar light to irradiate adsorbed MO molecules deep inside the cryogel to initiate their photo-degradation.

3.4 Photo-degradation mechanism of N-doped Q-NFC/TiO_2 cryogel

It is known that the catalytic activity of a photocatalyst is closely related to the band gap energy.[56] The band gap energy (E_g) of Ti species for the 10Ti–NFC and 10N10Ti–NFC cryogels was estimated from the Tauc plot of transformed Kubelka–Munk function *versus* $h\nu$ as expressed in the following eqn (6):[57]

$$(Ah\nu)^{1/2} \propto h\nu - E_g \quad (6)$$

where A is the absorption coefficient, ν is the frequency of the light, and h is Planck's constant.

From the UV-Vis diffuse reflectance spectra in Fig. 8a, the band gaps of 10Ti–NFC and 10N10Ti–NFC were calculated to be 2.76 eV and 2.64 eV, respectively, according to the formula for the band gap.[58] After nitrogen doping, the valence band edge exhibited 0.12 eV of red shift. Similarly, nitrogen-induced band gap narrowing results were observed for other nitrogen-doped titania materials.[47,59,60]

Also, the highest occupied molecular orbital (HOMO) level was calculated to be *ca.* −4.67 eV for 10N10Ti–NFC and −4.69 eV for 10Ti–NFC using the equation HOMO = $-(E_{ox}$ + 4.74) eV,[61] where the onset potential E_{ox} can be estimated from the cyclic voltammetry curve in Fig. 8b to be −0.07 and −0.05 V, respectively. Then, the lowest unoccupied molecular orbital (LUMO) energy levels can be calculated to be −1.97 eV for 10N10Ti–NFC and −2.07 eV for 10Ti–NFC by subtracting the optical band gap from the HOMO.[61,62] According to the literature,[63] the conduction band of bare anatase TiO_2 was reported to be −4.42 eV. Thus, when irradiated with solar light, the electron was allowed to be transferred from nitrogen to TiO_2 in the 10N10Ti–NFC. As shown in Fig. 8b, the oxidized electric current of 10N10Ti–NFC was also larger than that of 10Ti–NFC.

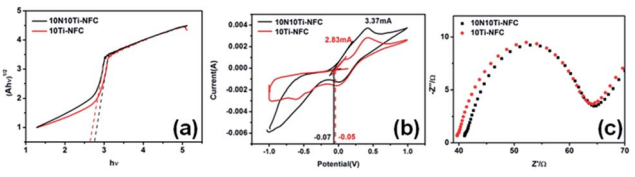

Fig. 8 (a) Optical energy band gaps, (b) cyclic voltammograms (CV), and (c) electrochemical impedance spectra (EIS) of 10NTi–10NFC and 10Ti–NFC.

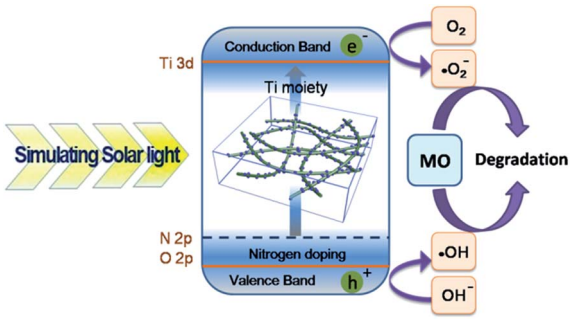

Fig. 9 The proposed photocatalytic mechanism diagram of N-doped TiO_2/Q-NFC cryogels.

These results clearly manifested the role of doped nitrogen in the MO photocatalytic process of TiO_2/Q-NFC hybrid cryogels. Fig. 8c shows the EIS measurement in Nyquist plots. One can note that the resistance of the working electrode is slightly reduced for 10N10Ti–NFC, reflecting a decrease in the solid state interface layer resistance and the charge transfer resistance across the solid–liquid interface of the 10N10Ti–NFC surface.[64] Electrons would be easily transferred due to the synergistic effect between TiO_2 and nitrogen, and lower the probability of e^-/h^+ recombination due to a higher electron transfer rate.[65]

The possible photocatalytic mechanism is shown in Fig. 9. First, electrons and holes pairs were formed under the irradiation of simulated solar light when the energy was equal to or higher than the band-gap of the cryogels. The excited-state electrons in the lowest unoccupied molecular orbital (LUMO) of Ti moieties will easily migrate into the LUMO of nitrogen. The radical $^{\bullet}O_2^-$ could be formed through the combination of photogenerated electrons with O_2 that was adsorbed on the surface of the cryogel. Meanwhile, the holes migrated toward the surface and reacted with H_2O to produce $^{\bullet}OH$, which was a strong oxidizing agent to decompose organic dyes. Consequently, more electrons and holes would be captured by oxygen or H_2O adsorbed on the surface of the hybrid cryogel to generate $^{\bullet}O_2^-$, $^{\bullet}OH$, or other active species which are responsible for the degradation of MO dye. Moreover, it should be pointed out that the cryogel possesses good adsorption ability, and it can supply more "reservation" room for MO molecules, and thus tends to facilitate the photocatalytic process.

4. Conclusions

In conclusion, nanofibrillated cellulose (Q-NFC) was synthesised and surface-functionalized with quaternary ammonium groups. Both TiO_2 photo-catalyst and N species were successfully co-incorporated into the Q-NFC backbone. Among various Q-NFC-based cryogels investigated in this study, the hybrid one loaded with N-doped TiO_2, displayed the optimum photo-degradation activity for MO dye under the irradiation of simulated solar light, although its adsorption abilities were somewhat lowered relative to pure Q-NFC. Furthermore, the excellent self-integrated removal efficiency for MO (more than

99%) and reusability during multiple adsorption/photodegradation cycles were observed for the N-doped hybrid cryogel with mechanical durability and recyclability. Its photodegradation mechanism was discussed in terms of its optical and electrochemical properties. The easily recyclable advantage of the Q-NFC based hybrid cryogel made it a promising reusable and eco-friendly alternative for the self-cleaning treatment of dye pollutants.

Acknowledgements

The authors are grateful for the financial support from the Public Welfare Projects of Zhejiang Province (2017C33113 & 2016C33029), Scientific Research Foundation of Zhejiang Agriculture & Forestry University (2013FR088), National Natural Science Foundation of China (51302109), and Natural Science Foundation of Jiangsu Province of China (BK20130144).

Notes and references

1 Z. Karim, A. P. Mathew, M. Grahn, J. Mouzon and K. Oksman, *Carbohydr. Polym.*, 2014, **112**, 668–676.
2 L. Jin, W. Li, Q. Xu and Q. Sun, *Cellulose*, 2015, **22**, 2443–2456.
3 A. K. Verma, R. R. Dash and P. Bhunia, *J. Environ. Manage.*, 2012, **93**, 154–168.
4 M. Rivera, M. Pazos and M. Sanromán, *J. Chem. Technol. Biotechnol.*, 2009, **84**, 1118–1124.
5 H. Ma, C. Burger, B. S. Hsiao and B. Chu, *Biomacromolecules*, 2011, **13**, 180–186.
6 Y. Qi, M. Yang, W. Xu, S. He and Y. Men, *J. Colloid Interface Sci.*, 2017, **486**, 84–96.
7 G. Mezohegyi, F. P. van der Zee, J. Font, A. Fortuny and A. Fabregat, *J. Environ. Manage.*, 2012, **102**, 148–164.
8 A. M. Atta, H. A. Al-Lohedan, Z. ALOthman, A. A. Abdel-Khalek and A. M. Tawfeek, *J. Ind. Eng. Chem.*, 2015, **31**, 374–384.
9 G. Crini and P.-M. Badot, *Prog. Polym. Sci.*, 2008, **33**, 399–447.
10 W. Maatar, S. Alila and S. Boufi, *Ind. Crops Prod.*, 2013, **49**, 33–42.
11 O. Hamdaoui, E. Naffrechoux, J. Suptil and C. Fachinger, *Chem. Eng. J.*, 2005, **106**, 153–161.
12 O. Hamdaoui and E. Naffrechoux, *J. Hazard. Mater.*, 2007, **147**, 381–394.
13 G. Z. Memon, M. Bhanger, M. Akhtar, F. N. Talpur and J. R. Memon, *Chem. Eng. J.*, 2008, **138**, 616–621.
14 F. Quignard, R. Valentin and F. Di Renzo, *New J. Chem.*, 2008, **32**, 1300–1310.
15 F. Zhang, W. Wu, S. Sharma, G. Tong and Y. Deng, *BioResources*, 2015, **10**, 7555–7568.
16 C. Wan, Y. Lu, C. Jin, Q. Sun and J. Li, *J. Nanomater.*, 2015, **2015**, 1–8.
17 R. Gavillon and T. Budtova, *Biomacromolecules*, 2007, **9**, 269–277.
18 M. Deng, Q. Zhou, A. Du, J. van Kasteren and Y. Wang, *Mater. Lett.*, 2009, **63**, 1851–1854.
19 M. Pääkkö, J. Vapaavuori, R. Silvennoinen, H. Kosonen, M. Ankerfors, T. Lindström, L. A. Berglund and O. Ikkala, *Soft Matter*, 2008, **4**, 2492–2499.
20 H. Sehaqui, Q. Zhou, O. Ikkala and L. A. Berglund, *Biomacromolecules*, 2011, **12**, 3638–3644.
21 H. Jin, Y. Nishiyama, M. Wada and S. Kuga, *Colloids Surf., A*, 2004, **240**, 63–67.
22 A. Dufresne, *Mater. Today*, 2013, **16**, 220–227.
23 M. Henriksson, G. Henriksson, L. A. Berglund and T. Lindström, *Eur. Polym. J.*, 2007, **43**, 3434–3441.
24 A. Pei, N. Butchosa, L. A. Berglund and Q. Zhou, *Soft Matter*, 2013, **9**, 2047–2055.
25 I. Besbes, S. Alila and S. Boufi, *Carbohydr. Polym.*, 2011, **84**, 975–983.
26 S. Kalia, S. Boufi, A. Celli and S. Kango, *Colloid Polym. Sci.*, 2014, **292**, 5–31.
27 D. Klemm, F. Kramer, S. Moritz, T. Lindström, M. Ankerfors, D. Gray and A. Dorris, *Angew. Chem., Int. Ed.*, 2011, **50**, 5438–5466.
28 K. T. Takashi Nishino, K. Nakamae, K. Saitaka, S. Itakura, J. Azuma and K. Okamura, *J. Polym. Sci., Part B: Polym. Phys.*, 1995, **33**, 611–618.
29 L. Panzella, L. Melone, A. Pezzella, B. Rossi, N. Pastori, M. Perfetti, G. D'Errico, C. Punta and M. D'Ischia, *Biomacromolecules*, 2016, **17**, 564–571.
30 W. Chen, Q. Li, Y. Wang, X. Yi, J. Zeng, H. Yu, Y. Liu and J. Li, *ChemSusChem*, 2014, **7**, 154–161.
31 Z. Cai, Z. Xiong, X. Lu and J. Teng, *J. Mater. Chem. A*, 2014, **2**, 545–553.
32 Y. Zhang, M. Huang, F. Li, H. Zhao and Z. Wen, *J. Mater. Sci.*, 2013, **48**, 6728–6736.
33 M. Kettunen, R. J. Silvennoinen, N. Houbenov, A. Nykänen, J. Ruokolainen, J. Sainio, V. Pore, M. Kemell, M. Ankerfors and T. Lindström, *Adv. Funct. Mater.*, 2011, **21**, 510–517.
34 M. A. Mohamed, W. Salleh, J. Jaafar, A. Ismail, M. A. Mutalib, N. Sani, S. Asri and C. Ong, *Chem. Eng. J.*, 2016, **284**, 202–215.
35 J. Han, C. Zhou, Y. Wu, F. Liu and Q. Wu, *Biomacromolecules*, 2013, **14**, 1529–1540.
36 Z. Zhang, G. Sèbe, D. Rentsch, T. Zimmermann and P. Tingaut, *Chem. Mater.*, 2014, **26**, 2659–2668.
37 R. T. Olsson, M. A. Samir, G. Salazar-Alvarez, L. Belova, V. Ström, L. A. Berglund, O. Ikkala, J. Nogues and U. W. Gedde, *Nat. Nanotechnol.*, 2010, **5**, 584–588.
38 X. Gao, S. R. Bare, J. Fierro, M. A. Banares and I. E. Wachs, *J. Phys. Chem. B*, 1998, **102**, 5653–5666.
39 R. Asahi, T. Morikawa, T. Ohwaki, K. Aoki and Y. Taga, *Science*, 2001, **293**, 269–271.
40 Y.-F. Shen, S. L. Suib, M. Deeba and G. Koermer, *J. Catal.*, 1994, **146**, 483–490.
41 M. Sundrarajan and A. Rukmani, *E-J. Chem.*, 2012, **9**, 1511–1517.
42 A. Shehap, *Egypt. J. Solid.*, 2008, **31**, 75–91.
43 D. Mahato, R. Prasad and B. Mathur, *Indian J. Pure Appl. Phys.*, 2009, **47**, 643.
44 J. Zhang, J. Zhang, L. Lin, T. Chen, J. Zhang, S. Liu, Z. Li and P. Ouyang, *Molecules*, 2009, **14**, 5027–5041.

45 T. Okpalugo, P. Papakonstantinou, H. Murphy, J. McLaughlin and N. Brown, *Carbon*, 2005, **43**, 153–161.
46 J. Wang, D. N. Tafen, J. P. Lewis, Z. Hong, A. Manivannan, M. Zhi, M. Li and N. Wu, *J. Am. Chem. Soc.*, 2009, **131**, 12290–12297.
47 S. Sakthivel, M. Janczarek and H. Kisch, *J. Phys. Chem. B*, 2004, **108**, 19384–19387.
48 Y. Li, Y. Jiang, S. Peng and F. Jiang, *J. Hazard. Mater.*, 2010, **182**, 90–96.
49 Q. Ling, J. Sun and Q. Zhou, *Appl. Surf. Sci.*, 2008, **254**, 3236–3241.
50 X. Chen, D.-H. Kuo and D. Lu, *Chem. Eng. J.*, 2016, **295**, 192–200.
51 L. Jin, Q. Sun, Q. Xu and Y. Xu, *Bioresour. Technol.*, 2015, **197**, 348–355.
52 A. J. Svagan, M. A. Samir and L. A. Berglund, *Adv. Mater.*, 2008, **20**, 1263–1269.
53 N. T. Cervin, C. Aulin, P. T. Larsson and L. Wågberg, *Cellulose*, 2012, **19**, 401–410.
54 M. Fumagalli, D. Ouhab, S. M. Boisseau and L. Heux, *Biomacromolecules*, 2013, **14**, 3246–3255.
55 X. He, K. B. Male, P. N. Nesterenko, D. Brabazon, B. Paull and J. H. Luong, *ACS Appl. Mater. Interfaces*, 2013, **5**, 8796–8804.
56 J. Schneider, M. Matsuoka, M. Takeuchi, J. Zhang, Y. Horiuchi, M. Anpo and D. W. Bahnemann, *Chem. Rev.*, 2014, **114**, 9919–9986.
57 L. Yoong, F. K. Chong and B. K. Dutta, *Energy*, 2009, **34**, 1652–1661.
58 S. U. Khan, M. Al-Shahry and W. B. Ingler, *Science*, 2002, **297**, 2243–2245.
59 S. Sakthivel and H. Kisch, *ChemPhysChem*, 2003, **4**, 487–490.
60 W. Wang, Y. Liu, J. Qu, Y. Chen and Z. Shao, *RSC Adv.*, 2016, **6**, 40923–40931.
61 C. Ma, L. Zhang, J. Zhou, X. Wang, B. Zhang, Y. Cao, P. Bugnon, M. Schaer, F. Nüesch and D. Zhang, *J. Mater. Chem.*, 2002, **12**, 3481–3486.
62 Y. J. Chang and T. J. Chow, *J. Mater. Chem.*, 2011, **21**, 3091–3099.
63 J. S. Lee, K. H. You and C. B. Park, *Adv. Mater.*, 2012, **24**, 1084–1088.
64 B.-L. He, B. Dong and H.-L. Li, *Electrochem. Commun.*, 2007, **9**, 425–430.
65 H. J. Yun, H. Lee, N. D. Kim and J. Yi, *Electrochem. Commun.*, 2009, **11**, 363–366.